Searching for models of thermo-chemical convection that explain probabilistic tomography
I. Principles and influence of rheological parameters

Frédéric Deschamps *, Paul J. Tackley

Institute of Geophysics, Swiss Federal Institute of Technology Zurich, HPP L8.1, 8093 Zurich, Switzerland

ABSTRACT

Recent seismological observations indicate that strong lateral density anomalies, likely due to compositional anomalies, are present in the deep mantle. We aim to identify models of thermo-chemical convection that can generate strong thermo-chemical density anomalies. For this, we explore the model space of thermo-chemical convection, determine the thermal and chemical density distributions predicted by these models, and compare their power spectra against those from probabilistic tomography. We conduct 3D-Cartesian numerical experiments using STAG3D, in which we prescribed an initial layer of dense material at the bottom of the system. We focus on the parameters of the viscosity law, including the compositional ($R\mu_c$), 660 km ($R\mu_{660}$), depth ($R\mu_z$), and thermal ($R\mu_T$) viscosity contrasts, and report strong differences in the pattern of thermo-chemical convection depending on the values of these ratios. For small (≤ 0.1) values of $R\mu_c$ dense and regular materials quickly mix, whereas for large ($\geq 10^2$) values of $R\mu_c$ the layer of dense material remains stable. Only moderate (0.1–10) $R\mu_c$ predict patterns that can maintain chemical density anomalies that fit seismic observations over long periods of time. A large ($\geq 10^2$) $R\mu_{660}$ acts as a filter for dense material, maintaining strong lateral chemical density anomalies in the lower mantle, but the power spectra of these distributions do not fit seismic tomography in the long term. A large ($\geq 10^4$) $R\mu_T$ maintains strong density anomalies everywhere in the lower mantle, including pools of dense material at the bottom of mantle, which fits seismic tomography well. A successful model of thermo-chemical convection (in the sense that it fits seismological observations well) might thus include a moderate (0.1–10) compositional density contrast and/or a strong ($\geq 10^4$) thermal viscosity contrast. The influence of other important parameters, including the buoyancy ratio, the Clapeyron slope at $d = 660$ km and the fraction of dense material, are explored in a companion paper.

1. Introduction

More than three decades have passed since the first numerical models of mantle convection were designed (e.g., Moore and Weiss, 1973; McKenzie et al., 1974). However, the mode of mantle convection is still highly debated. A major difficulty in finding a successful model is that the Earth's mantle includes numerous complexities compared to classical Rayleigh–Bénard convection (e.g., among the most important, viscosity variations with temperature, phase transitions, mode of heating). In addition, a successful model must be consistent with observations and constraints from various fields, including geochemistry, seismology, gravimetry, and mineral physics.

A major constraint, which arose and gained increasing support in the past decade, is the presence of strong density variations in the lower mantle (Ishii and Tromp, 1999; Resovsky and Trampert, 2003; Trampert et al., 2004), likely due to chemical variations (Forte and Mitrovica, 2001; Karato and Karki, 2001; Saltzer et al., 2001; Deschamps and Trampert, 2003). Thermo-chemical convection might thus be a key ingredient for a successful model of mantle convection. Analogical experiments (Olson and Kincaid, 1991; Davaille, 1999; Jellinek and Manga, 2002) and numerical models (Christensen and Hofmann, 1994; Kellogg et al., 1999; Tackley, 1998b; Tackley, 2002) observed a variety of flow patterns, from strong stratification to more complex structures, depending on the chemical density contrast between the dense and regular material and the fluid properties.

The increase in complexity of convection models opened new perspectives in the comparison between geophysical observations and models of mantle convection. Global tomography provides so far the best constraints on the 3D structure of the lower mantle, but

---

* Corresponding author. Tel.: +41 446336906; fax: +41 446331065.
E-mail address: frederic.deschamps@erdw.ethz.ch (F. Deschamps).

its interpretation is not unambiguous (Trampert and van der Hilst, 2005). Two crucial ingredients are independent constraints on the mass density, and a careful equation of state modeling (Deschamps and Trampert, 2003; Trampert et al., 2004). In a previous paper (Deschamps et al., 2007), we developed a method to test density distributions predicted by thermo-chemical convection against those from probabilistic tomography, which we applied to snapshots from various runs. These comparisons showed that a stable layer of dense material does not explain probabilistic tomography. Piles of dense material entrained upward provide a better explanation, but are short-lived structures that develop early in the run history. They may not explain the present tomography.

Searching for successful model(s) of mantle convection requires an extensive exploration of the model space of thermo-chemical convection over time sequences comparable to the age of the Earth, and careful comparison with available geophysical constraints. An important question is how to maintain density anomalies in the bottom of the mantle for a long period of time. Previous studies showed that a dense layer is able to survive thermal convection over 4.5 Gyr and more, provided that the buoyancy ratio is large enough (Tackley, 2002; Samuel and Farnetani, 2003; Zhong and Hager, 2003; van Thienen et al., 2005). However, a stable layer of dense material with no or weak topography does not fit seismic tomography (Deschamps et al., 2007). In this paper, we extend the approach of Deschamps et al. (2007). We then explore the influence of the parameters of the viscosity law on the flow pattern and the distribution of thermal and chemical density anomalies, and compare these distributions against those from probabilistic tomography (Trampert et al., 2004).

Parameters of the viscosity law control the viscosity variations with depth, temperature and composition. Depth- and temperature-dependence were introduced to model the pressure and thermal dependence of mantle minerals creeping laws (e.g., Weertman, 1970). Additional complexities of creep laws include the grain-size dependence, the role of fluids, and the stress exponent. Temperature-dependent viscosity attracted a particular attention (e.g., Christensen, 1984; Ogawa et al., 1991; Moresi and Solomatov, 1995). High viscosity contrasts due to temperature variations result in a stagnant lid regime (e.g., Davaille and Jaupart, 1993; Moresi and Solomatov, 1995; Deschamps and Sotin, 2000) that is relevant to model convection in the mantles of Venus (Solomatov and Moresi, 1996) and icy satellites (Deschamps and Sotin, 2001), but fails to explain plate tectonics regime as observed on the Earth. Self-consistent modeling of plate tectonics requires the prescription of more complex rheologies at the top of the system (Tackley, 1998a). When studying whole mantle convection, such complex rheologies can be neglected, and a Newtonian rheology, associated with diffusion creep, is well suited (Karato and Wu, 1993). Temperature- and depth-dependent viscosity remain however important ingredients, in particular for thermo-chemical convection (McNamara and Zhong, 2004). In addition, both geoid (Hager and Richards, 1989) and post-glacial rebound (Nakada and Lambeck, 1989; Forte and Mitrovica, 1996) data suggest that the lower mantle is more viscous than the upper mantle by about one order of magnitude. Finally, it is reasonable to consider that dense and regular materials have different viscosities.

Other important parameters include the Rayleigh number, the buoyancy ratio, and the Clapeyron slope of the 660 km phase transition. We explore these parameters in a companion paper (Deschamps and Tackley, submitted for publication).

2. Experimental setup

We conducted numerical experiments using a 3D-Cartesian version of STAG3D (Tackley, 1998b; Tackley, 2002), which solves the non-dimensional conservative equations of mass, momentum, energy, and composition for an anelastic, compressible fluid with an infinite Prandtl number. Calculations are made on staggered grids of $128 \times 128 \times 64$ points, with aspect ratio equal to 4. Grids are vertically refined at the top and at the bottom of the box. Scalar and vectorial quantities are calculated at the center and on the sides of each cell, respectively. At each time step, the conservative equations are solved using a Jacobi relaxation method. In addition, to speed up the convergence of the momentum equation, we used a multigrid algorithm (e.g., Stüben and Trottenberg, 1982). Time-stepping (in conservations of energy and composition) is achieved by an explicit MPDATA (Smolarkiewicz, 1984) algorithm for advective terms, and a second-order finite difference scheme for diffusive and other terms. Runs are stopped at a non-dimensional time $t = 0.0106$, which correspond to a dimensional time of 4.5 Gyr. Previous studies (e.g., Davies, 2002) performed runs over longer periods of time to account for the possibility that convection was more vigorous in the past. In many cases, however, a quasi-stationary pattern (i.e., the average altitude of dense particles, Eq. (6), and the RMS of velocity are oscillating around constant values) is reached before the end of the run, and extending the run further in time would not significantly modify the thermal and chemical structures.

All boundaries are free-slip. The system is cooled on the top and heated both from below and from within. The heating rate for dense material is increased by a factor 10 compared to regular material, and the heating rate of the mantle is adjusted to give a total heat production equivalent to a heat flux of 65 mW/m^2. Because the MORB source region appears depleted in heat-producing elements, it is reasonable to assume that the concentration in radiogenic elements is higher in dense material that in regular material (Kellogg et al., 1999). The value of the compositional heating ratio (RH_c) we imposed is somewhat arbitrary, and one may wonder about the influence of RH_c on the mode of convection. We explored values of RH_c in the range 10^{-1} to 10^3, and found that the influence of RH_c is small compared to that of other parameters. The flow patterns of these cases are similar to that for the reference case, the time averaged of the RMS velocity are nearly constant around 1300, and the estimated mixing times (defined in Section 4.1) vary between 5.7×10^{-3} and 4.8×10^{-3}. This result contrasts with a recent study in 2D-Cartesian geometry (van Thienen et al., 2005), which reports a moderate but significant dependence on RH_c. This discrepancy might be explained by the difference in geometry.

The chemical field is modeled using 10 million tracer particles of two types, one for the regular material, and one for the dense material (Tackley and King, 2003). Tracers are advected following a 4th order Runge–Kutta method. The number of particles of dense material is fixed by prescribing the fraction of dense material, X. Dense particles are initially distributed in the bottom of the system, leading to a dense layer of (non-dimensional) thickness h_{DL}. Numerically, h_{DL} is equal to the initial volume fraction of dense material, X. The concentration of dense particles C is measured in each cell, and varies between $C = 0$ and $C = 1$ for a cell fully filled with regular and dense material, respectively. The density contrast between dense and regular material, $\Delta\rho_c$, creates negative buoyancy that acts against the positive thermal buoyancy. The relative strength of chemical buoyancy is usually measured by the buoyancy ratio

$$B \equiv \frac{\Delta\rho_c}{\Delta\rho_T}, \tag{1}$$

where $\Delta\rho_T = \alpha_S \rho_S \Delta T_S$, α_S and ρ_S are the thermal expansion and density at zero pressure, and ΔT_S the superadiabatic temperature difference across the system. In the present study, we fixed the fraction of dense material and buoyancy ratio to $X = 10\%$ and $B = 0.2$, respectively. Taking $\alpha_S = 5.0 \times 10^{-5}$ K^{-1}, $\rho_S = 3300$ kg m^{-3},

and $\Delta T_S = 2500$ K, the density contrast between dense and regular material is thus $\Delta \rho_c = 82.5$ kg cm^{-3}.

Viscosity depends on temperature, depth, and composition. Depth-dependence consists of an exponential increase with depth, and a viscosity jump $R\mu_{660}$ at $d = 660$ km depth (non-dimensional depth $z = 0.228$). The exponential increase is controlled by a non-dimensional parameter V_a, which models the activation volume. Temperature-dependence is exponential and controlled by a non-dimensional parameter E_a representing the activation energy. Finally, the compositional dependence is also exponential and controlled by the ratio between the viscosities of the dense and regular materials, $R\mu_c$. By analogy with the thermal and depth dependences, it is convenient to define a chemical potential Λ_a, which in our case is numerically equal to $\ln(R\mu_c)$. The non-dimensional viscosity (with respect to the surface viscosity, μ_S) can thus be written:

$$\begin{cases} \mu(z, T, C) = \exp[V_a z - E_a T + \Lambda_a C] & z < 0.228 \\ \mu(z, T, C) = \Delta \mu_{660} \exp[V_a z - E_a T + \Lambda_a C] & z > 0.228 \end{cases}, \quad (2)$$

where T is the non-dimensional temperature, and z the non-dimensional depth.

Because the fluid viscosity, thermal expansion, thermal diffusivity and density are allowed to vary throughout the system, the definition of the Rayleigh number is non-unique. As input, we prescribe the surface Rayleigh number:

$$Ra_S = \frac{\alpha_S g \rho_S \, \Delta T_S D^3}{\mu_S \kappa_S}, \quad (3)$$

where g is the acceleration of gravity, D the mantle thickness, and κ_S the surface thermal diffusivity. The surface Rayleigh number remains constant during the entire run (surface values of all parameters are assumed constant with time), and in all the calcu-

lations shown in this paper we prescribed $Ra_S = 10^8$. In contrast, the effective Rayleigh number Ra_{eff}, calculated with the properties of the material of the well-mixed interior, does vary with time. The value and time evolution of the effective Rayleigh number strongly depends on the model parameters. In the reference case, Ra_{eff} drops by 15% after the onset of instability of the dense layer, and remains constant around 10^6 during the rest of the run. For a large (≥ 10) compositional viscosity contrasts, Ra_{eff} is smaller, around 10^5, and slightly increases with time. The effect of temperature-dependent viscosity is more significant. In the case $R\mu_T = 10^6$, for instance, Ra_{eff} increases from 1.4×10^5 to 2.2×10^5 during the run duration. Variations in time of the surface Rayleigh number (due to variations in the surface viscosity, density, and thermal expansion) are however not accounted for in our calculations. This may induce small biases in the evolution of the system, in particular if the Rayleigh number was larger in the past (Davies, 2002).

Compressibility induces an additional sources and sinks of heat that are controlled by the dissipation number. Again, the definition of this number is non-unique. The dissipation number as a function of depth is given by

$$Di(d) = \frac{\alpha(d)gD}{C_P}, \quad (4)$$

where C_P is the heat capacity, which we assumed to be constant with depth. In all our experiments, the surface and volume average dissipation numbers are $Di_S = 1.2$ and $\langle Di \rangle = 0.43$, respectively. A phase transition at $d = 660$ km is implemented, but we imposed a zero Clapeyron slope.

Conservative equations involve reference profiles for thermo-dynamic parameters, including density, thermal expansion, and temperature. Reference profiles are calculated using an appropriate thermodynamic model (Tackley, 1996; Tackley, 1998b), and scaled

Table 1
Parameters and scalings

Parameter	Symbol	Value	Units	Non-dimensional
Non-dimensional parameters				
Surface Rayleigh number	Ra_S			10^8
Buoyancy ratio	B			0.2
Volume fraction of dense material	X			0.10
Initial thickness of the dense layer	h_{DL}			0.10
Surface dissipation number	Di_S			1.2
Volume average dissipation number	Di			0.43
Total internal heating	H_c	65	mW m^{-2}	25
Compositional heating ratio	RH_c			10
Physical and thermo-dynamical parameters (dimensional)				
Acceleration of gravity	g	9.81	m s^{-2}	1.0
Mantle thickness	D	2891	km	1.0
Superadiabatic temperature difference	ΔT_S	2500	K	1.0
Reference geotherm	T_{as}	1600	K	0.64
Surface density	ρ_S	3300	kg m^{-3}	1.0
Density jump at $d = 660$ km	$\Delta \rho_{660}$	400	kg m^{-3}	0.1212
Surface thermal expansion	α_S	5.0×10^{-5}	K^{-1}	1.0
Surface thermal diffusivity	κ_S	6.24×10^{-7}	m^2 s^{-1}	1.0
Heat capacity	C_P	1200	J kg^{-1} K^{-1}	1.0
Surface conductivity	k_S	3.0	W m^{-1} K^{-1}	1.0
Surface Grüneisen parameter	γ_S	1.091		
Viscosity law				
Surface thermal viscosity	μ_S	1.6×10^{21}	Pa s	1.0
Viscosity ratio at $d = 660$ km	$R\mu_{660}$	1.0–300		
Compositional viscosity ratio	$R\mu_c$	3.2×10^{-3}–10^3		
Depth viscosity ratio	$R\mu_z$	1.0–10^4		
Thermal viscosity ratio	$R\mu_T$	1.0–10^7		
Dimensional scalings				
Velocity	v	1.0	cm yr^{-1}	1468
Time	t	424	Gyr	1.0
Heat flux	Φ	2.6	mW m^{-2}	1.0
Internal heating rate	H	2.72×10^{-13}	W kg^{-1}	1.0

with respect to their surface value (except temperature, which is scaled to ΔT_S). The thermodynamic parameters we used to build the reference state are listed in Table 1, together with other physical parameters and scalings. Note that we assumed a density jump at $d = 660$ km, but not at $d = 410$ km.

To avoid the transient phase in which the dense layer heats up, the temperature field is initialized with a geotherm taken from 2D calculations that have reached secular equilibrium, to which we added random 3D perturbations. 2D calculations have similar boundary conditions as the 3D cases, and include a dense layer at the bottom. This initial condition does not influence the flow evolution after the onset of instability of the dense layer.

3. Stability of the dense layer

The layer of dense material at the bottom of the system creates negative buoyancy that stabilizes it. To generate instabilities from this layer, thermal buoyancy must overcome the chemical negative buoyancy. This can be achieved by heating the system during a long enough period of time. Howard (1966) pointed out that a thermal boundary layer becomes unstable if its thickness exceeds a critical value that is determined from a local Rayleigh number. Furthermore, the onset time for the rise of instabilities depends on the properties of the system. A larger viscosity increases the critical thickness of the thermal boundary layer, thus delaying the onset of instability. It is also useful to define a proper Rayleigh number for the dense layer:

$$Ra_{DL} = \frac{\alpha \rho g \, \Delta T_{DL} h_{DL}^3}{\mu_{DL} \kappa}, \tag{5}$$

and compare it to a critical Rayleigh number, estimated from linear stability analysis. LeBars and Davaille (2002) and Jaupart et al. (2007) performed such analysis and showed that the critical Rayleigh number mainly depends on the buoyancy ratio and, to a lesser extent, on the compositional viscosity contrast.

From Eq. (5), it is clear that a small (large) value of the viscosity of the dense layer is decreasing (increasing) Ra_{DL}. A compositional viscosity contrast smaller than 1 (the dense material is less viscous than the regular material) will oppose the action of dense material and decrease the time for the onset of instability. On the contrary, a compositional viscosity contrast larger than 1 or an increase of viscosity with depth will enhance the stability of the layer of dense material. Because our calculations include more complexities (depth- and temperature-dependent viscosity, com-

pressibility) than the linear stability analysis in LeBars and Davaille (2002) and Jaupart et al. (2007), their results might not valid in our case. However, it is worth noting that for $B = 0.2$, they found a critical Rayleigh number of about 125. Taking $Ra = 10^8$, $h_{DL} = 0.1D$, and $\Delta T_{DL} = 0.5 \Delta T_S$, Ra_{DL} is larger than the critical Rayleigh number if the viscosity of the dense layer is smaller than the surface viscosity by a ratio of about 400.

To estimate the time of the onset of instability of the dense layer (t_{onset}), we calculated the average non-dimensional altitude of dense material:

$$\langle h_c \rangle = \frac{1}{V} \int_V (1 - z) C(x, y, z) \, \mathrm{d}V, \tag{6}$$

as a function of time. Initially, $\langle h_c \rangle$ is equal to half the thickness of the dense layer, h_{DL}, i.e., it is numerically equal to $X/2$, where X is the volume fraction of dense material. As long as the dense layer is stable $\langle h_c \rangle$ remains equal to $X/2$, but when the dense layer gets unstable it increases. Time evolutions of $\langle h_c \rangle$ (Section 5, Figs. 3a, 6a and 9a), clearly show that t_{onset} increases with increasing compositional (Rμ_c), 660 km (Rμ_{660}), and depth (Rμ_z) viscosity contrasts. Note that for R$\mu_c = 10^2$, the dense layer remains stable during the entire run. t_{onset} also increases with increasing thermal viscosity contrast (Rμ_T), but the layer gets unstable even for large (at least 10^7) values of Rμ_T.

4. Processing the numerical results

4.1. Estimated mixing time

Mixing time is estimated from the time evolution of the variance in the distribution of composition, var(t). Following previous studies (Ferrachat and Ricard, 2001; Olson et al., 1984), we first defined the function:

$$e(t) = 1 - \frac{\mathrm{var}(t)}{\mathrm{var}(t = 0)}, \tag{7}$$

and its time integral over the duration of the run, $f(t_{run})$. The function $e(t)$ varies between zero at $t = 0$ and its statistical limit

$$e_{max} = 1 - \frac{N - 1}{n_{part}}, \tag{8}$$

where n_{part} and N are the number of particle tracers and the number of cells, respectively. The integral $f(t_{run})$ varies between $f_{min} = 0$, for a bottom layer that remains strictly stable, and $f_{max} = e_{max} t_{run}$, in
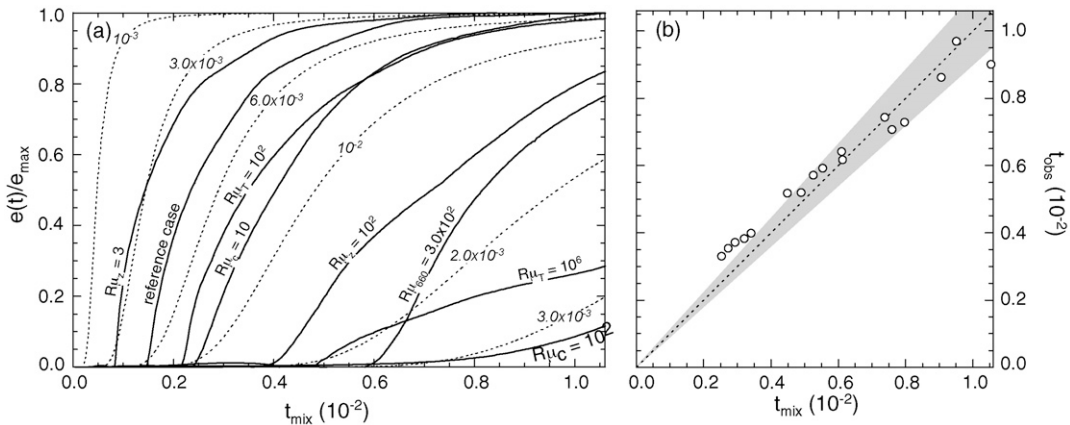

Fig. 1. Estimating the mixing time. (a) Comparison between the function $\xi^2 \exp(\xi)/[\exp(\xi) - 1]^2$, where $\xi = (t_0/t)^{1.5}$ (dotted curves; the value of t_0 is indicated with italic numbers), and the ratio $e(t)/e_{max}$ for various cases (thick plain curves; the case considered is indicated on each curve). (b) Comparison between the mixing time estimated from Eq. (9), and the 'observed' mixing time, defined as the time at which the function $e(t)$ (Eq. (7)) reaches 92% of its statistical limit. The gray shaded area covers ±10% around the estimated mixing time.

the (hypothetical) case of a system instantaneously homogenized at $t = 0$. Interestingly, $e(t)$ fits reasonably well the family of functions $g(\xi) = c\xi^2 \exp(\xi)/[\exp(\xi) - 1]^2$, where c is a constant and $\xi = (t_0/t)^{1.5}$, except for large values of $R\mu_{660}$ and $R\mu_T$ (Fig. 1a). The function $g(\xi)$ reaches 92% of its maximum value at time $t = t_0$ and tends towards c when t goes to infinity. Note that exponential functions are also used to estimate the mantle degassing time by convective mixing (Coltice, 2005). It is not clear why $e(t)$ is well described by $g(\xi)$. This function is however well known in statistical physics. It describes the temperature dependence of the specific heat of a collection of atoms (modeled by harmonic oscillators) distributed between discrete energy levels. As the temperature of the assembly of atoms increases, a larger number of energetic levels are populated, and the specific heat (which measures the increase in the entropy of the system for a given increment of temperature), increases. We

suggest the following analogy. The distribution of particles of dense material is obviously discrete (due to the finite difference scheme we use), and the initial condition (the particles of dense material are all distributed in a basal layer) may correspond to a fundamental, frozen state (all atoms are in the lower energy level). As time increases, convective flow allows the particles of dense material to reach a larger number of locations, and the function $e(t)$ (which measures the time evolution of the mixing efficiency of the system, and therefore of its entropy) increases. To estimate the mixing time t_{mix}, we thus solve the equation:

$$f(t_{run}) = e_{max} \int_0^{t_{run}} \xi^2 \frac{\exp(\xi)}{[\exp(\xi) - 1]^2} \, dt, \quad \xi = \left(\frac{t_{mix}}{t}\right)^{1.5}, \tag{9}$$

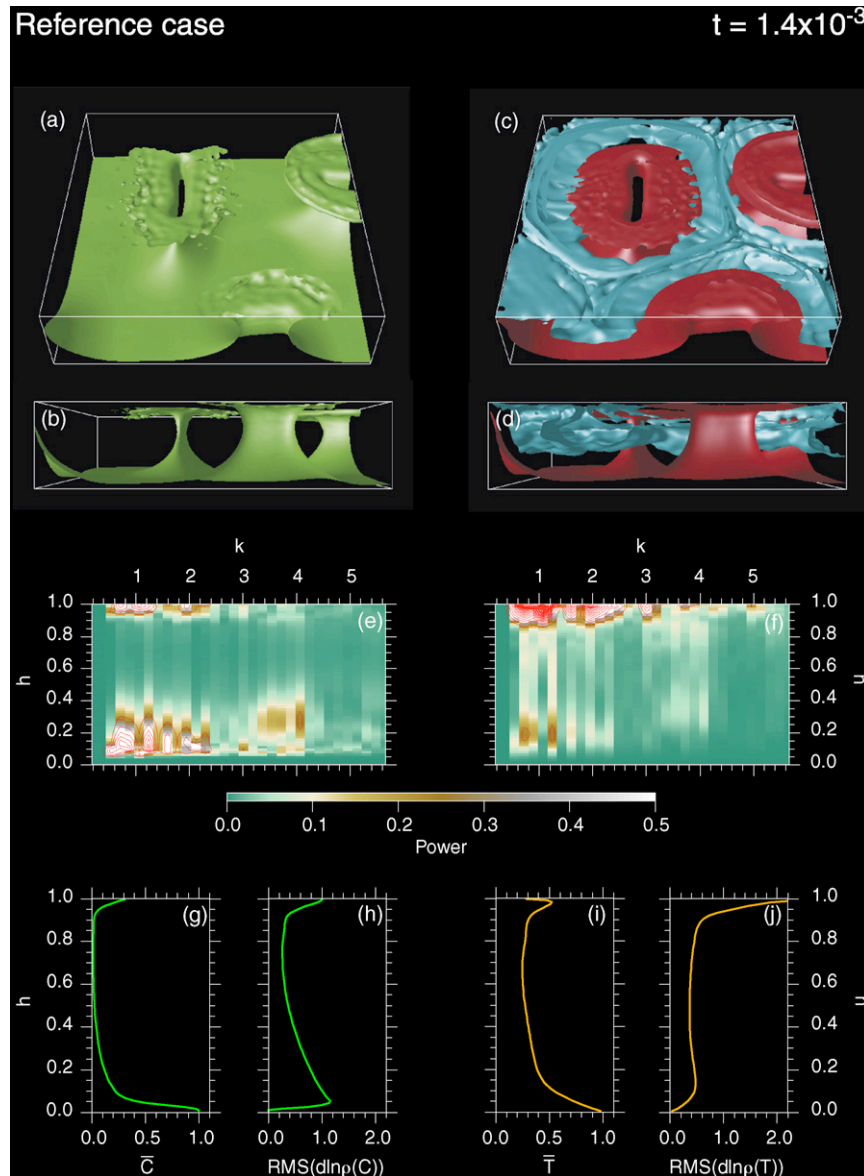following a Newton–Raphson method.

Fig. 2. Snapshot of the reference case at $t = 1.4 \times 10^{-3}$ (0.6 Gyr). Parameters of the viscosity law are $R\mu_c = 10^{-2}$, $R\mu_{660} = 30$, $V_a = 2.303$ ($R\mu_z = 10$), and $E_a = 0$ ($R\mu_T = 1$). (a and b) Isosurface of the concentration in dense particle, with contour level $C = 0.5$. (c and d) Isosurfaces of the non-dimensional temperature (relative to average), with contour levels $T - \langle T \rangle = -0.15$ (blue) and $T - \langle T \rangle = 0.15$ (red). (e) Spectral heterogeneity map (SHM) of the chemical density anomalies, $d \ln \rho_c$ (Eq. (11)). (f) SHM of the thermal density anomalies, $d \ln \rho_T$ (Eq. (10)). SHMs are plotted with both a color scale and contour levels (red curves, interval is 0.2). h is the non-dimensional altitude. (g) Profile of the horizontally average concentration in dense particle, $\bar{C}$. (h) Profile of the RMS of the chemical density anomalies $d \ln \rho_c$. (i) Profile of the horizontally average non-dimensional temperature, $\bar{T}$. (j) Profile of the RMS of the thermal density anomalies $d \ln \rho_T$. (For interpretation of the references to color in this figure legend, the reader is referred to the web version of the article.)

An advantage of Eq. (9), compared to previous studies (Ferrachat and Ricard, 2001; Olson et al., 1984), is to provide estimates of the mixing time even if the mixing is not completed at the end of the run. However, this approach fails to predict a mixing time when the dense layer remains stable, e.g., for a large compositional viscosity contrast ($R\mu_c = 30$ and more). Similarly, our estimates are strongly underestimated if the mass transfer around $d = 660$ km is reduced (large values of $R\mu_{660}$), or if pools of dense material generate at the bottom of the system (large values of $R\mu_T$). In cases for which mixing is completed before the end of the run, the value of t_{mix} predicted by Eq. (9) agrees very well with the observed time at which $e(t)$ reaches 92% of the statistical limit e_{max} (Fig. 1b).

4.2. RMS flow velocity

The RMS of the flow velocity, RMS(v), does not provide a direct measure of the mixing, but is indirectly related to it. The faster the flow, the more efficient the mixing. Another measure of the mixing efficiency is the bulk Lagrangian strain rate (Coltice, 2005). For instance, in the case of a 2D-Cartesian fluid, Coltice (2005) established scaling laws of the processing time as a function of this strain rate. Flow velocity is controlled by various parameters, including the parameters of the viscosity law. All other parameters being equal, a fluid flows more slowly as its viscosity increases. Thus, if the viscosity of the dense material increases, the velocity of thermo-chemical plumes decreases, and mixing gets less efficient. It is difficult to predict *a priori* the influence of the various viscosity variations on RMS(v). In the case of a temperature-dependent viscosity, for instance, the top of the system is more viscous and flows slower than average, but the bottom is less viscous and flows faster than average. In most cases (Section 5, Figs. 3b, 6b and 9b), RMS(v) sharply increases immediately after the onset of instability, reaches a peak, and decreases again to an intermediate values around which it oscillates during the rest of the run. The amplitude of the maxi-

mum of RMS(v) strongly depends on the type and amplitude of the viscosity variation. Overall, the time average of RMS(v), $\langle RMS(v) \rangle_t$, provide a good estimate of the characteristic amplitude of the flow velocity for each case (Section 5, Figs. 3d, 6d and 9d).

4.3. Lateral chemical and thermal heterogeneities

Thermo-chemical convection provides distributions of temperature and composition that we use to compute relative density variations. At each depth, the lateral density anomalies due to thermal and compositional variations around the average temperature $\bar{T}(z)$ and fraction of dense particles $\bar{C}(z)$ at this depth are (Deschamps et al., 2007)

$$d \ln \rho_T = \frac{\alpha_{ref}[T - \bar{T}(z)]}{1 - \alpha_{ref}[\bar{T}(z) - T_{ref}]}, \tag{10}$$

and

$$d \ln \rho_c = -\alpha_S \, \Delta T_S \frac{B[C - \bar{C}(z)]}{1 + \alpha_S \, \Delta T_S B \bar{C}(z)}. \tag{11}$$

Profiles of the RMS of $d \ln \rho_T$ and $d \ln \rho_c$ provide the first hints of the thermo-chemical structure. A stable layer of dense material results in a RMS that peaks around the interface between regular and dense material, and is zero elsewhere. Piles of dense material rising from a dense layer predict a RMS of $d \ln \rho_c$ that increases with depth down to the top of the dense layer. If dense and regular materials are well mixed, the RMS of $d \ln \rho_c$ is constant with depth and close to zero. Unfortunately, uncertainties and the vertical parameterization of tomographic models are such that the comparison of RMS profiles from tomography and thermo-chemical convection alone cannot provide a full diagnostic for the mantle convection (Deschamps et al., 2007).
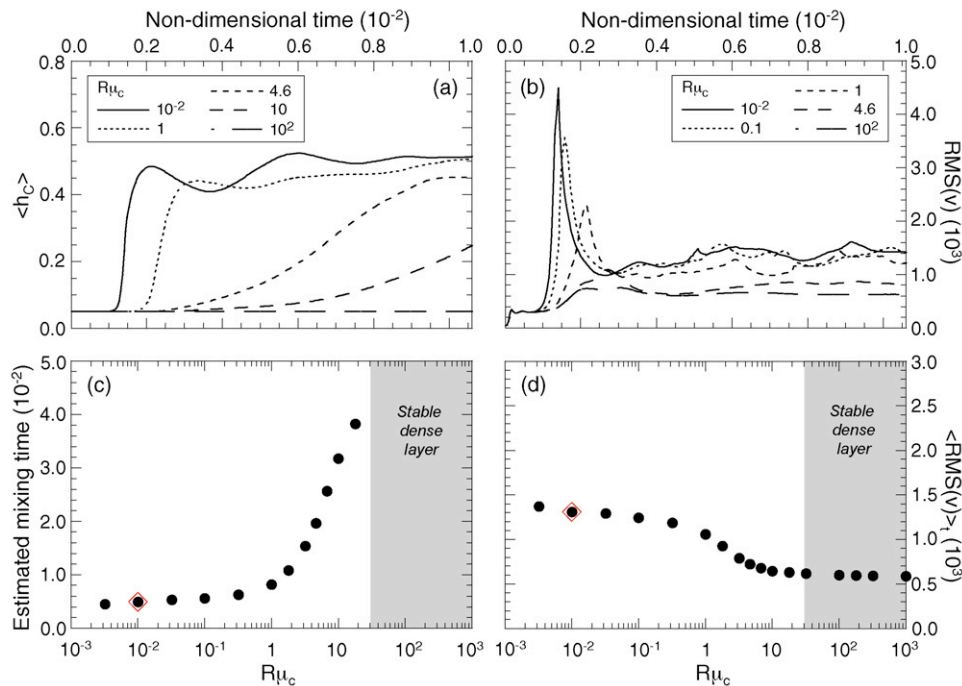

Fig. 3. Influence of the compositional viscosity ratio, $R\mu_c$. (a) Average altitude of dense material, $\langle h_c \rangle$ (Eq. (6)), as a function of time and for various values of $R\mu_c$. (b) RMS of the flow velocity as a function of time and for various values of $R\mu_c$. (c) Estimated mixing time as a function of $R\mu_c$. For $R\mu_c \geq 30$, dense layer is stable during the entire run, and we cannot give estimate of the mixing time. (d) Time average RMS of the flow velocity as a function of $R\mu_c$. In plots (c) and (d), the reference case is indicated by the red diamond. (For interpretation of the references to color in this figure legend, the reader is referred to the web version of the article.)

More detailed information can be inferred from spectral heterogeneity maps (SHMs, Tackley et al., 1994) of $d \ln \rho_T$ and $d \ln \rho_c$. The SHM of a given 3D distribution is obtained by calculating the 2D Fourier expansion of this distribution at each depth and plotting the resulting power spectrum as a function of the wave number ($k = \sqrt{k_x + k_y}$) and the depth.

4.4. Comparison with probabilistic tomography

We decided to test our models of thermo-chemical convection against probabilistic tomography (Resovsky and Trampert, 2003; Trampert et al., 2004) because this model includes a distribution of density anomalies in the lower mantle. Density anomalies are
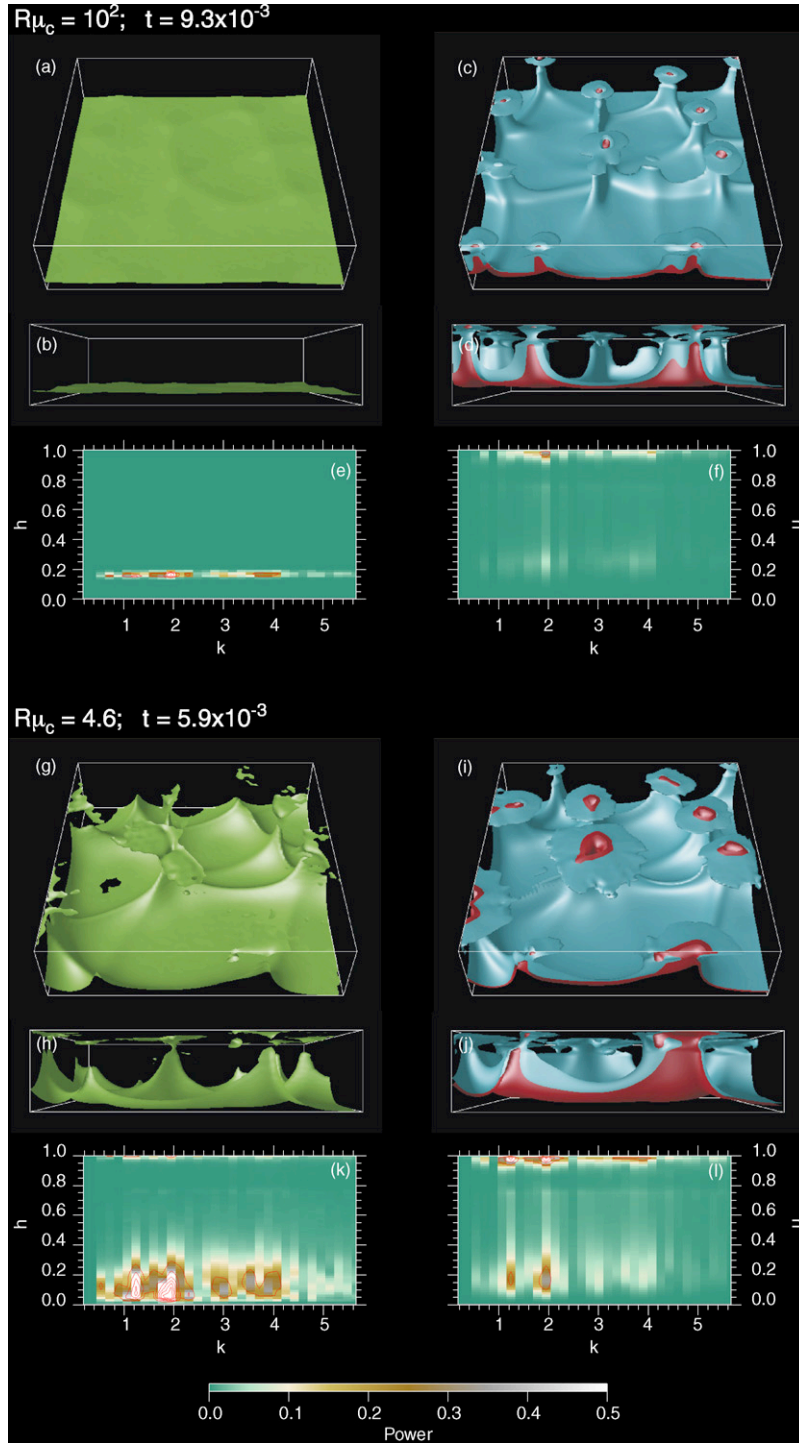

Fig. 4. (a–f) Snapshot of the case $R\mu_c = 10^2$ at $t = 9.3 \times 10^{-3}$ (2.5 Gyr). Other parameters are as in the reference case. (a and b) Isosurface of the concentration in dense particle, with contour level $C = 0.5$. (c and d) Isosurfaces of the non-dimensional temperature (relative to average), with contour levels $T - \langle T \rangle = -0.05$ (blue) and $T - \langle T \rangle = 0.05$ (red). (e) Spectral heterogeneity map (SHM) of the chemical density anomalies, $d \ln \rho_c$ (Eq. (11)). (f) SHM of the thermal density anomalies, $d \ln \rho_T$ (Eq. (10)). SHMs are plotted with both a color scale and contour levels (red curves, interval is 0.2). h is the non-dimensional altitude. (g–l) Snapshot of the case $R\mu_c = 4.6$ at $t = 5.9 \times 10^{-3}$ (3.9 Gyr). Other parameters are as in the reference case. Plots description is similar to that for plots (a–f). (For interpretation of the references to color in this figure legend, the reader is referred to the web version of the article.)

essential to resolve the trade-off that exists between temperature and composition. Furthermore, probabilistic tomography provides full probability density functions (rather than mean values only) for anomalies in density and seismic velocity at each point of the model.

A convenient way to compare the distributions of density anomalies predicted by tomography and thermo-chemical convection is to compare their power spectra. Global tomographic models, including probabilistic tomography from Trampert et al. (2004) (hereafter referred to as RT246g), are developed in spherical harmonics, and relevant comparisons requires that we appropriately sum up the Fourier spectra of density anomalies obtained

by thermo-chemical convection over the wave number k. Assuming that the power per surface unit is the same in the Fourier and harmonic expansions, the signal contained in spherical harmonic degree ℓ is obtained by summing the wave numbers that satisfies (Chevrot et al., 1998)

$$\ell + \frac{1}{2} \le ka \le \ell + \frac{3}{2}, \quad k = \sqrt{k_x + k_y}, \tag{12}$$

where a is the Earth's radius, and k_x and k_y the wave number along the x-axis and y-axis. Following this rule, one can expand density anomalies from thermo-chemical convection up to spherical harmonic 32. This is far enough for compar-
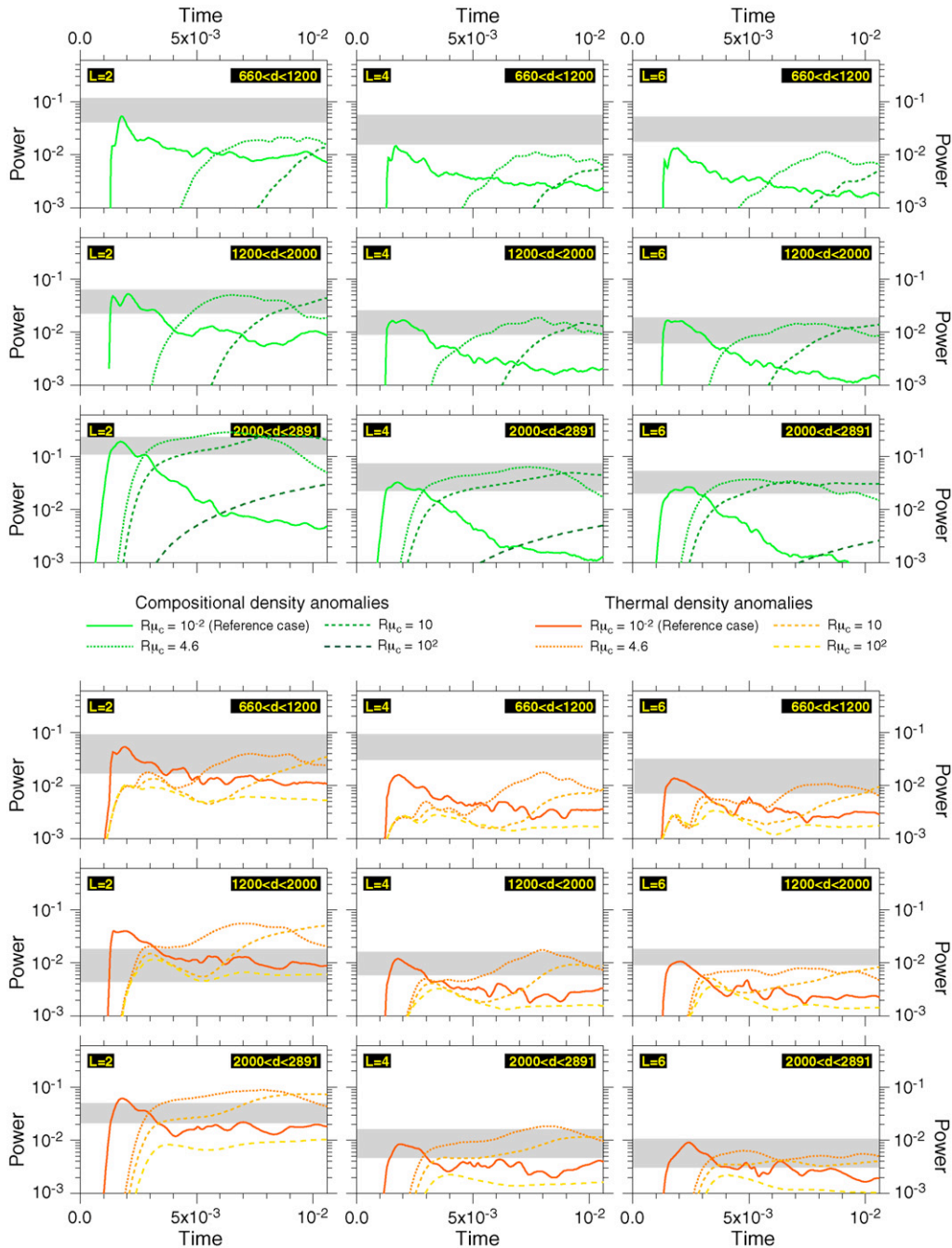

Fig. 5. Power of chemical (three top rows) and thermal (three bottom rows) density anomalies as a function of time and for various values of the chemical viscosity ratio, $R\mu_c$. Anomalies are averaged within three layers ($660 \le d \le 1200$ km, $1200 \le d \le 2000$ km, and $2000 \le d \le 2891$ km), and we considered three spherical harmonics ($L = 2$, $L = 4$, and $L = 6$). Gray bands indicate the power spectrum predicted by RT246g within twice its standard deviation.

ison with RT246g, which contains degrees 2, 4 and 6 only. Furthermore, one must vertically average the density anomalies from thermo-chemical convection according to the radial parameterization of RT246g. This includes two layers in the upper mantle ($24 \leq d \leq 410$ km and $410 \leq d \leq 660$ km), and three in the lower mantle ($660 \leq d \leq 1200$ km, $1200 \leq d \leq 2000$ km, and $2000 \leq d \leq 2891$ km). Note that because compositional anomalies are parameterized in terms of iron and perovskite anomalies (Trampert et al., 2004), the comparison with RT246g is meaningful only in the lower mantle.

5. Model space search: viscosity law parameters

To illustrate the method described in Section 4, we studied the influence of the parameters of the viscosity law (Eq. (2)) on the convective flow and on the efficiency of mixing. We define a reference case, and vary one parameter at a time, other parameters having values similar to those of the reference case. The surface Rayleigh number, fraction of dense material, and buoyancy ratio are the same for all the experiments reported in this paper, with $Ra_S = 10^8$, $X = 0.1$ and $B = 0.2$, respectively. We performed 46 runs in total, but only display snapshots from a few runs. Additional snapshots and movies from all cases are available as supplementary online material or by the authors on demand.

5.1. Reference case

For comparisons, we defined a reference case with the following properties. Viscosity varies with depth ($V_a = 2.303$, corresponding to a bottom to top viscosity ratio equal to 10), but not with temperature ($E_a = 0$). The viscosity jump at the upper/lower mantle boundary ($R\mu_{660}$) is equal to 30, and the dense material is less viscous than the regular material by two orders of magnitude ($R\mu_c = 10^{-2}$). As discussed below, this case generates large thermo-chemical plumes that lead to efficient mixing between dense and regular material. It may thus be used as a reasonable reference to better understand the influence of each parameter.

In this case, the time for the onset of instability of the dense layer (t_{onset}) is around 0.9×10^{-3} (i.e., a dimensional time around 0.4 Gyr). Large plumes are generated from the dense layer, entraining dense and hot material upwards (Fig. 2, plots a–d). This pattern is associated with strong chemical heterogeneities at the bottom and, to a lesser extent, at the top of the system (Fig. 2, plots e and h). Strong thermal heterogeneities are also present at the top of the system (Fig. 2, plots f and j). The power spectrum of chemical anomalies is dominated by large-scale structures with (non-dimensional) wave number up to $k = 2.5$ (Fig. 2e). Thermal anomalies have a wider spectrum, with wave number up to $k = 3.5$ (Fig. 2f). The distributions of these anomalies agree well with those from probabilistic tomography (Deschamps et al., 2007). However, piles are generated early in the run history and remain stable for a short period of time only, in the range $10^{-3} \leq t \leq 2.0 \times 10^{-3}$ (0.42–0.84 Gyr). During this episode, most of the dense layer is swept out. Thermal plumes, in contrast, remain present until the end of the run. Piles are thus an efficient way to mix dense and regular material, with an estimated mixing time $t_{mix} = 5.0 \times 10^{-3}$ (2.1 Gyr). An important consequence is that the amplitude of chemical density anomalies rapidly decreases with time.

5.2. Compositional viscosity contrast

We first explored the influence of the viscosity contrast between the dense and regular materials, varying $R\mu_c$ in the range 3.2×10^{-3}–10^3. Based on the variations of $\langle \mathrm{RMS}(v) \rangle_t$ and t_{mix}, we identify three regimes.

For $R\mu_c \leq 0.1$, the dense layer reaches the onset of instability within a short time (Fig. 3a). As in the reference case, we observe thermo-chemical plumes, but their size and velocity slightly decrease with increasing $R\mu_c$, and they remain present for a longer time. $\langle \mathrm{RMS}(v) \rangle_t$, slowly decreases (from ~1400 to ~1200) with increasing $R\mu_c$ (Fig. 3d). The mixing time is thus slightly increasing, but is always smaller than the time of the run (Fig. 3c). Again, piles are associated with strong lateral density anomalies, but these anomalies sharply decrease in amplitude with time, as
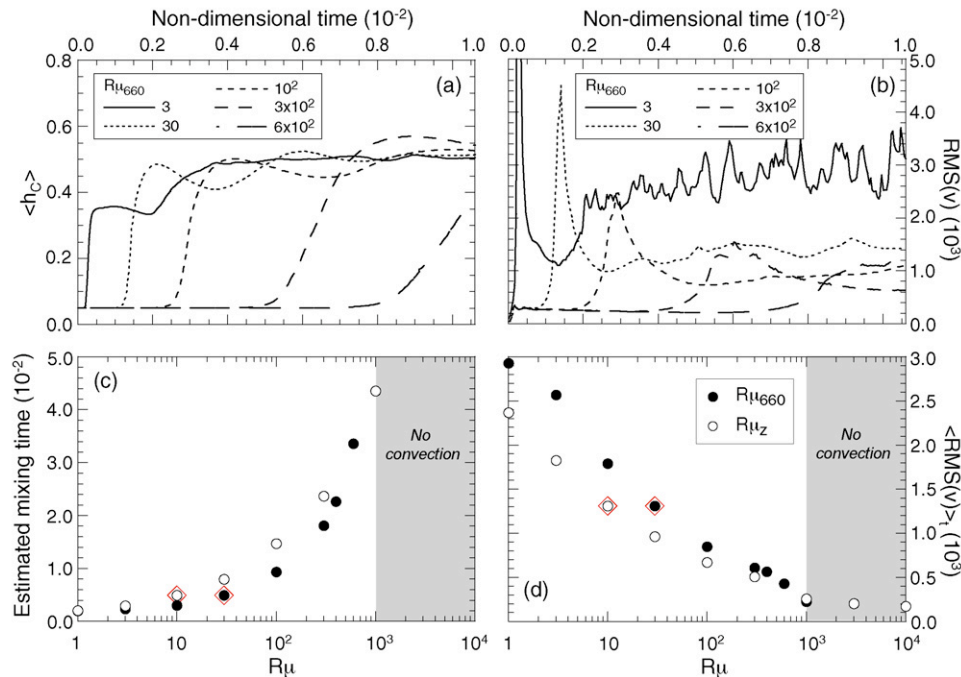

Fig. 6. Same as Fig. 3, but for various values of the viscosity ratio at $d = 660$ km, $R\mu_{660}$. Plots (c) and (d) also display the estimated mixing time and average RMS of the flow velocity for the depth viscosity ratio, $R\mu_z$ (open circles).

dense and regular material get mixed. The spherical harmonics power spectra of density anomalies fit RT246g well during a short period of time, but strongly disagree with them in the long term (Fig. 5, plain curves).

For $R\mu_c \geq 30$, the layer of dense material remains stable over long periods of time (Fig. 4, plots g and h). The layer of regular material is unstable with respect to thermal convection, and small

plumes rises from a thermal boundary layer located at the top of the dense material (Fig. 4, plots i and j). These thermal plumes entrain small amounts of dense material upwards, but thermal erosion is a slow process and is not completed before the end of the run. Lateral chemical anomalies are present, but strongly localised around the boundary between the dense and regular materials (Fig. 4k). Whatever the time, models with a stable layer of dense material do not fit
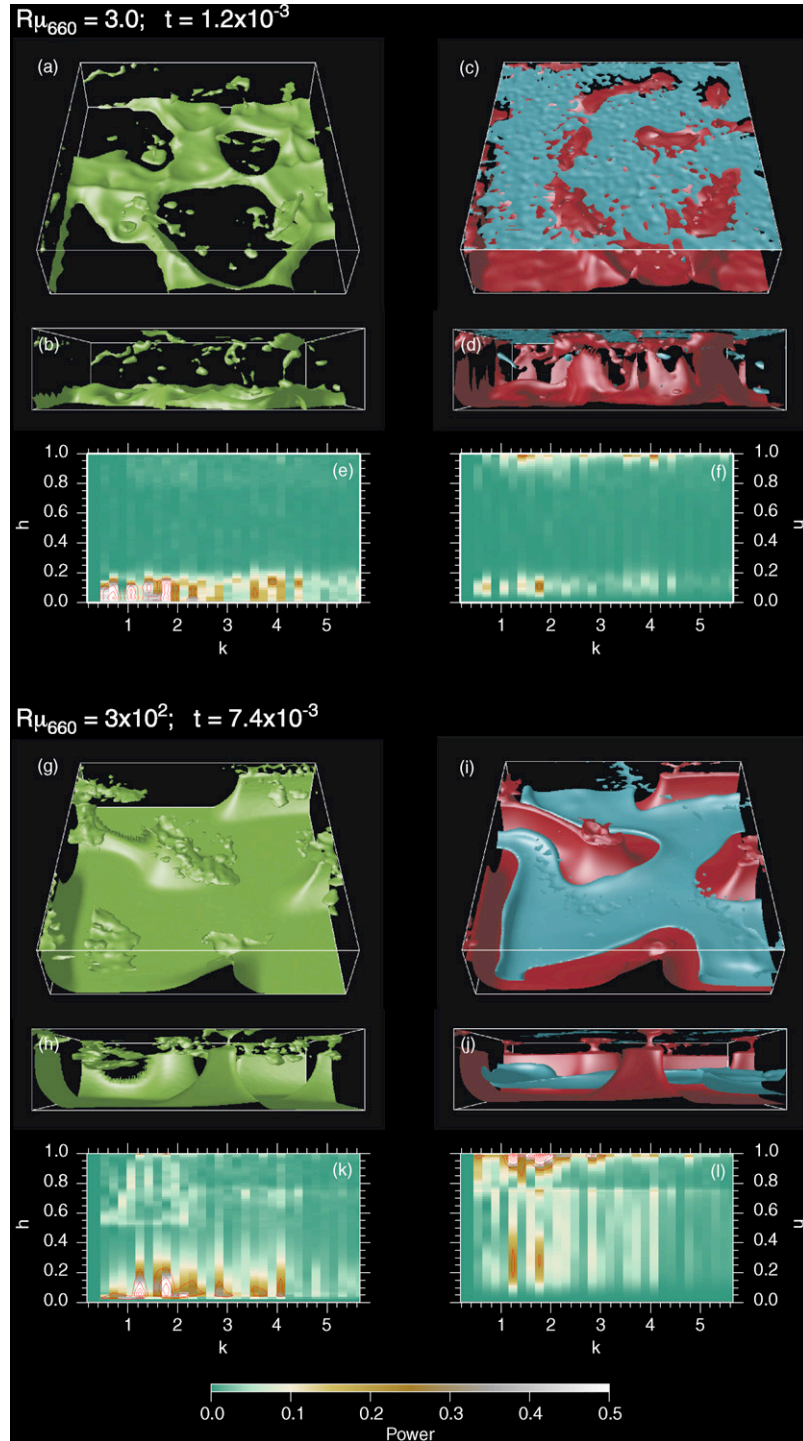

Fig. 7. (a–f) Snapshot of the case $R\mu_{660} = 3.0$ at $t = 1.2 \times 10^{-3}$ (0.5 Gyr). Other parameters are as in the reference case. Plots description is similar to that in plots (a–f) of Fig. 4. In plots (c) and (d), contour levels for temperature isosurfaces are $T - \langle T \rangle = -0.125$ (blue) and $T - \langle T \rangle = 0.075$ (red). (g–l) Snapshot of the case $R\mu_{660} = 3.0 \times 10^2$ at $t = 7.4 \times 10^{-3}$ (3.1 Gyr). Other parameters are as in the reference case. Plots description is similar to that in plots (a–f) of Fig. 4. In plots (i) and (j), contour levels for temperature isosurfaces are $T - \langle T \rangle = -0.2$ (blue) and $T - \langle T \rangle = 0.2$ (red). (For interpretation of the references to color in this figure legend, the reader is referred to the web version of the article.)

RT246g (Fig. 5, long dashed curves). In the layers $660 \leq d \leq 1200$ km and $1200 \leq d \leq 2000$ km, the power of chemical density anomalies is negligible. In the layer $2000 \leq d \leq 2891$ km, it slowly increases with time, but never reaches the value observed by RT246g.

For intermediate (0.1–10) values of $R\mu_c$, we observe transitional patterns, in which small fingers of dense, viscous, material are entrained upwards by thermal plumes (Fig. 4, plots a and b). The number and size of thermal plumes (Fig. 4, plots c and d) are intermediate between those observed for high and low $R\mu_c$. t_{onset} increases (Fig. 3a), whereas $\langle RMS(v) \rangle_t$ drops by ~ 500 (Fig. 3d). The thermo-chemical plumes remain stable for a longer period of time. The estimated mixing time sharply increases with increasing $R\mu_c$ (Fig. 3c). Interestingly, this pattern implies strong lateral anomalies of composition at the bottom of the system (Fig. 4e). The Fourier

power spectra are wider than in the reference case, and we observe strong anomalies up to $k = 4.2$. More importantly, these anomalies are maintained for a long period of time, and agree with seismic tomography in the long term. By the end of the run, the spherical harmonics power spectra of thermal density anomalies still fit RT246g reasonably well (Fig. 5, dotted and short-dashed curves), although some discrepancies remain in the layer 660–1200 km for all degrees of the chemical density anomalies, and for the degree 4 of the thermal density anomalies.

Three important conclusions can be drawn from this series of experiments. First, an increase in compositional viscosity contrast favours the development of small-scale structures. This observation is consistent with linear theory for Rayleigh–Taylor instabilities, which predict that plumes size and spacing increase as the plumes
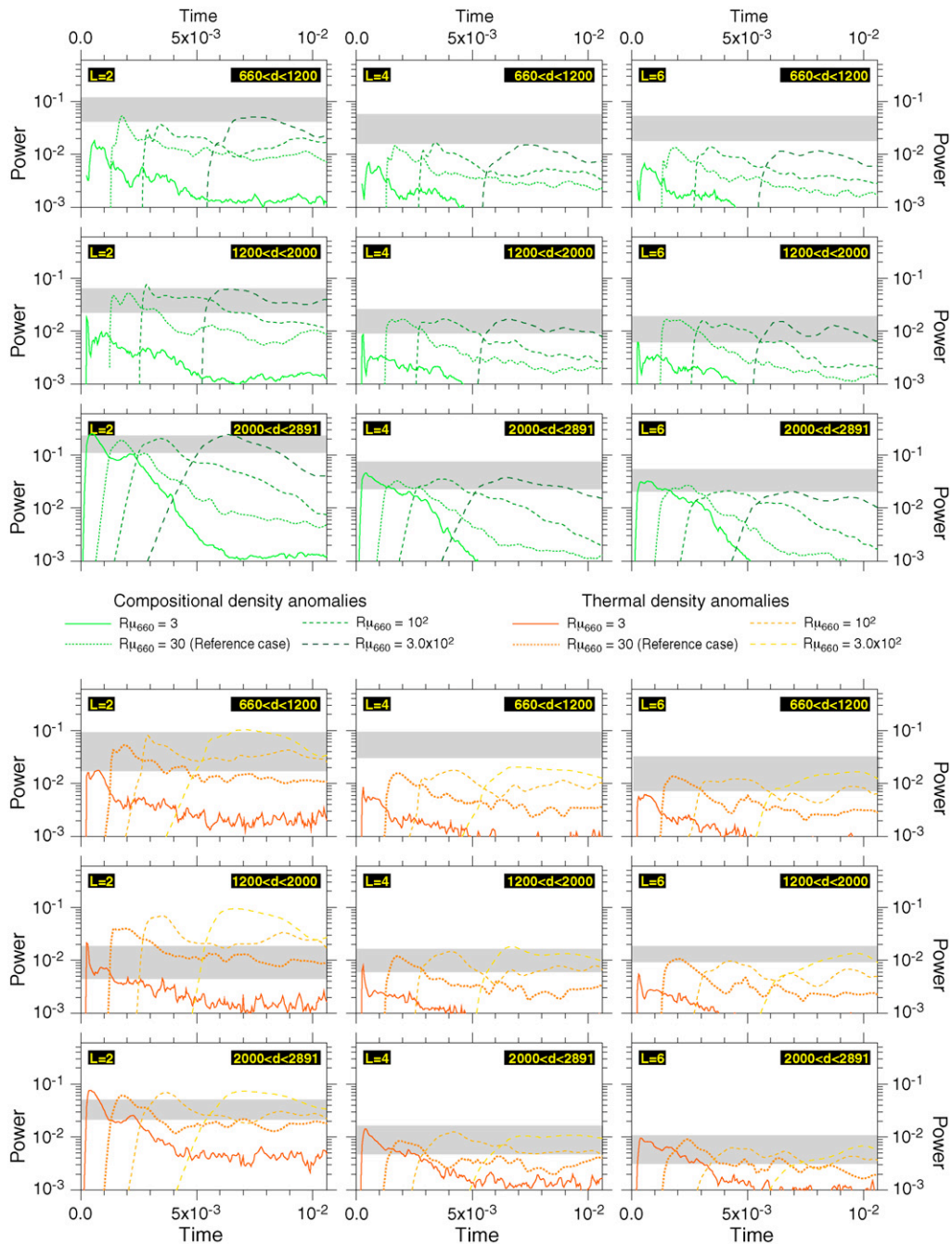

Fig. 8. Same as Fig. 5, but for various values of the viscosity ratio at $d = 660$ km, $R\mu_{660}$.

viscosity decrease (Whitehead and Luther, 1975). Second, thermo-chemical plumes, and therefore lateral density anomalies, can be maintained for longer period of time as $R\mu_c$ increases. In other words, the mass flux within thermo-chemical plumes decreases with increasing $R\mu_c$. Again, this observation agrees with linear theory for Rayleigh–Taylor instabilities. Finally, for high enough values of $R\mu_c$ (30 and more), the dense layer remains stable during the whole run, i.e., for period of time comparable to the age of the Earth.

5.3. Depth-dependent viscosity

Viscosity variations with depth are controlled by an exponential increase with depth and a viscosity contrast at $d = 660$ km ($z = 0.228$). We independently explored the influence of these two parameters, varying $R\mu_{660}$ between 1 and 10^3, and $R\mu_z$ between 1 and 10^4 ($0 \leq V_a \leq 9.210$). Note that for $R\mu_{660}$ and $R\mu_z$ larger than critical values, which, in this series of experiments, are around 10^3 and 3.0×10^3, respectively, the whole system is stable and does not convect.

For small (≤ 10) values of $R\mu_{660}$ we observe fast, small-scale plumes entraining dense material upwards (Fig. 7, plots c and d). t_{onset} is small (Fig. 6a), around 5.0×10^{-4} (0.2 Gyr) for $R\mu_{660} = 3$, and the plume velocity reaches extremely large values, up to 10^4 (~ 6.8 cm/yr) (Fig. 6b). Similarly, $\langle RMS(v) \rangle_t$ is large, up to 3000 for $R\mu_{660} = 1$ (Fig. 6d). The dense layer mixes with the regular material, with $t_{mix} \leq 3.0 \times 10^{-3}$ (2.7 Gyr) (Fig. 6c). In the early stages, interconnected ridges of dense material are present at the bottom of the system (Fig. 7, plots a and b). These structures are associated with moderate density anomalies up to $k = 4.5$ (Fig. 7e), which are very short-lived and poorly fit RT246g (Fig. 8).

On the contrary, for $R\mu_{660} \geq 10$, large-scale structures dominate the flow. For moderate (10–50) values of $R\mu_{660}$, we observe large thermo-chemical plumes surrounded by downwelling sheets, similar to those seen in the reference case (Fig. 2). For larger (10^2 to 6.0×10^2) values of $R\mu_{660}$, large-scale structures are still present, but we note major changes in the flow pattern (Fig. 7g–j). The average flow velocity is strongly attenuated (Fig. 6b and d). Thermo-

chemical plumes are interconnected with ridges of hot, dense material. More importantly, the viscosity contrast strongly attenuates the upward mass transfer. Thermo-chemical plumes dramatically narrow as they cross the 660 km boundary. In addition, t_{onset} sharply increases with $R\mu_{660}$ (Fig. 6a). The mixing of dense and regular materials is thus severely inhibited. Note that in this case, the variance in the concentration of dense particle does not fit well the function $\xi^2 \exp(\xi)/[\exp(\xi) - 1]^2$ (Fig. 1a), and that our estimates of the mixing time are underestimated. Strong lateral chemical density anomalies are present in the lower part of the system (Fig. 7k). Thermal density anomalies are also present, but mostly concentrate below the surface (Fig. 7l). Compared to those obtained for moderate $R\mu_{660}$, these anomalies are smaller in amplitude, but they are maintained for longer periods of time. Globally, their power spectra fit RT246g well (Fig. 8, short and long dashed curves). However, the power spectra of chemical density anomalies slowly decrease with time and, in the long term, disagree with RT246g.

The convective pattern sensitivity to $R\mu_z$ is similar to that to $R\mu_{660}$, with some differences (Fig. 6c and d, open circles). For small (≤ 5) values of $R\mu_z$, the flow is dominated by fast, small-scale structures, which quickly mix dense and regular materials. For large (10^2 to 10^3) $R\mu_z$, thermo-chemical plumes progressively narrow with altitude, and anomalies of density at the bottom of the system are maintained for long period of time.

Increasing $R\mu_{660}$ (or $R\mu_z$) has two main effects. First, the dense layer gets more viscous, and thus more stable (Fig. 6a). Second, it favours the development of large-scale structures, as pointed out in previous studies (Bunge et al., 1996; Tackley, 1996). Furthermore, for large ($\geq 10^2$) values of $R\mu_{660}$, the transfer of dense material around 660 km depth is strongly attenuated, and density anomalies are maintained in the lower part of the system for moderate periods of time.

5.4. Temperature-dependent viscosity

Finally, we performed numerical experiments for thermal viscosity contrasts between 1 ($E_a = 0$) and 10^7 ($E_a = 16.118$). t_{onset}
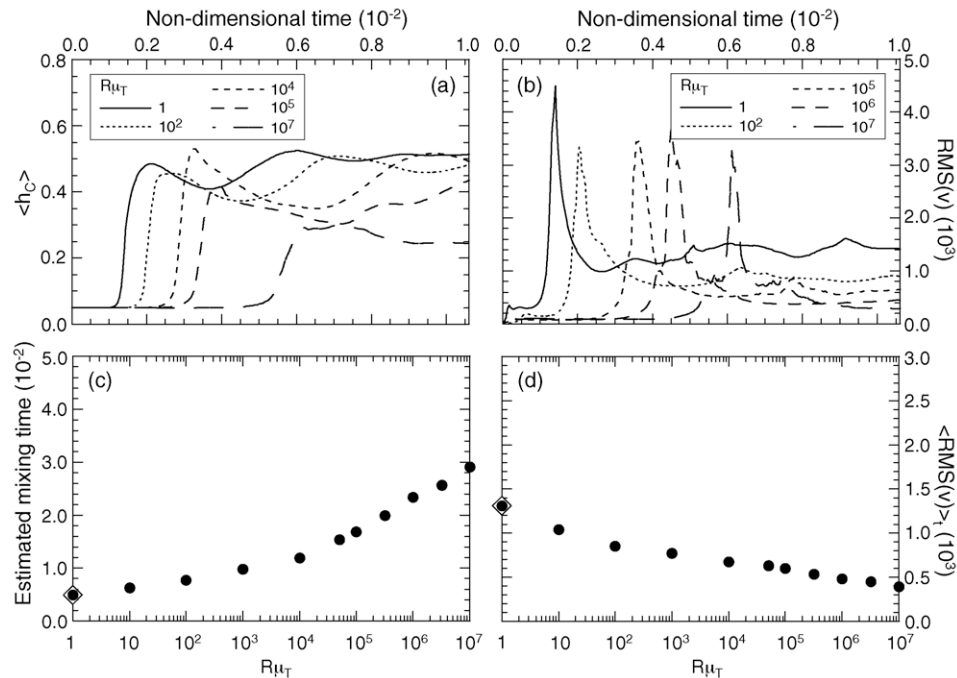

Fig. 9. Same as Fig. 3, but for various values of the thermal viscosity ratio, $R\mu_T$.

increases with $R\mu_T$ (Fig. 9a), but is smaller than the run duration in all cases. The flow pattern immediately after the onset of instability depends very little on $R\mu_T$. In all cases, we see large thermo-chemical plumes surrounded by downwelling sheets. The peak of RMS(v) that follows the onset of instability remains approximately constant with $R\mu_T$ (Fig. 9b).

In later stages, however, the flow patterns strongly differ, depending on $R\mu_T$. Furthermore, RMS(v) decreases with increasing $R\mu_T$. Overall, $\langle RMS(v) \rangle_t$ drops by a factor 3 between $R\mu_T = 1$ and $R\mu_T = 10^7$ (Fig. 9d) (note that this decrease also account for the increase in t_{onset}). For $R\mu_T \leq 10^4$, dense material concentrates in narrow ridges and is rapidly entrained upwards. Convection is efficient enough to sweep out and mix the layer of dense material within the run duration (Fig. 9c). McNamara and Zhong (2004) observed similar patterns and evolutions in spherical geometry. For larger values of $R\mu_T$, on the contrary, pools of dense material are generated at the foot of hot thermal plumes and survive thermal convection during the entire run (Fig. 10, plots a–d). Note that we do not observe such pools for $R\mu_T \leq 10^4$, even temporarily. Again, the formation of pools severely inhibits the mixing of dense and regular materials, and the mixing times calculated by Eq. (9) are strongly underestimated. The presence of pools induces strong chemical density anomalies with wave number up to $k = 4.0$ throughout the lower half of the system (Fig. 10, plots e and h). Moderate thermal density anomalies are also present at the bottom of the system, but the largest thermal anomalies are found below the surface (Fig. 10, plots f and j).

Globally, the spherical harmonics power spectra of thermal and chemical density anomalies fit RT246g better as $R\mu_T$ increases (Fig. 11). In particular, for $R\mu_T \geq 10^5$ the power spectra of chemical density anomalies in the bottom and intermediate layers remain close to those of RT246g over long periods of times. Some important discrepancies remain in the layer 660–1200 km, where the power of chemical density anomalies for all spherical harmonic degrees strongly decrease after reaching a peak, and the power of thermal density anomalies for degree 4 remain too small at any time.
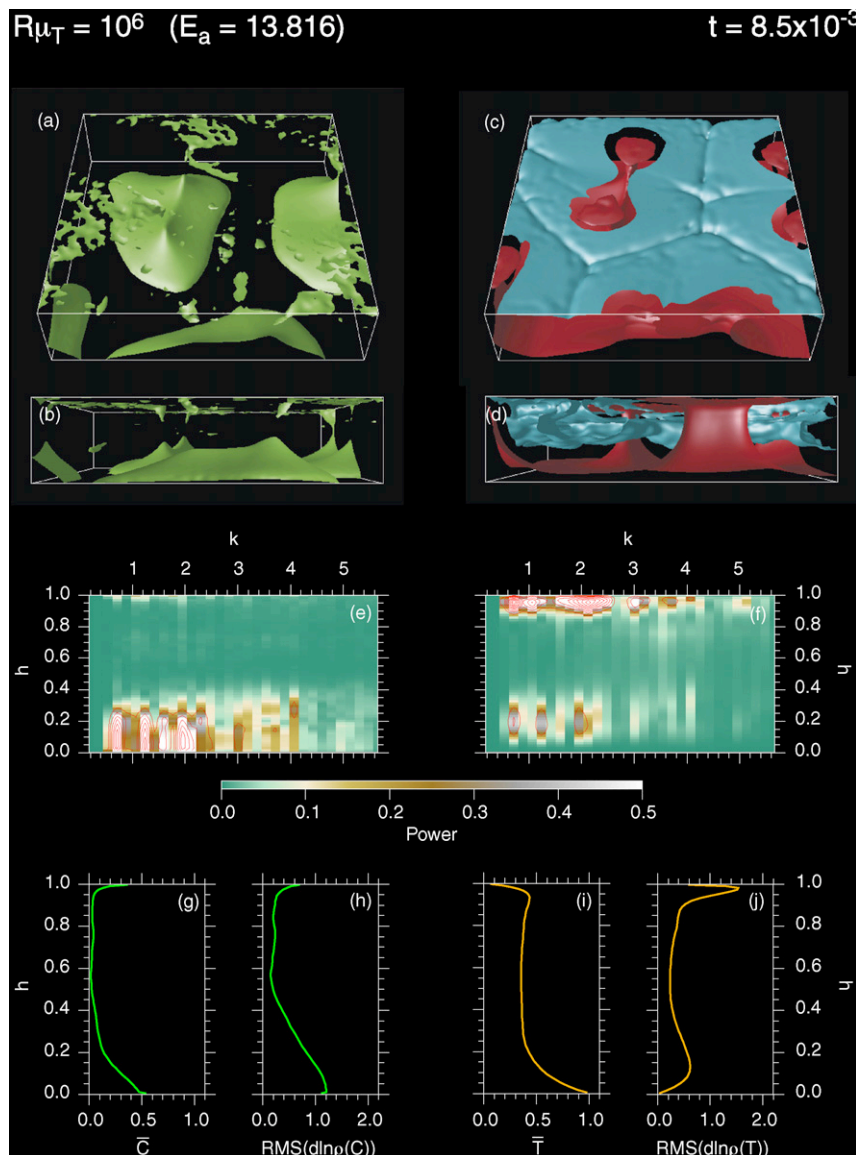

Fig. 10. Snapshot of the case $R\mu_T = 10^6$ at $t = 8.5 \times 10^{-3}$ (3.6 Gyr). Other parameters are as in the reference case. Plots description is similar to that in Fig. 2. In plots (c) and (d), contour levels for temperature isosurfaces are $T - \langle T \rangle = -0.25$ (blue) and $T - \langle T \rangle = 0.15$ (red). (For interpretation of the references to color in this figure legend, the reader is referred to the web version of the article.)
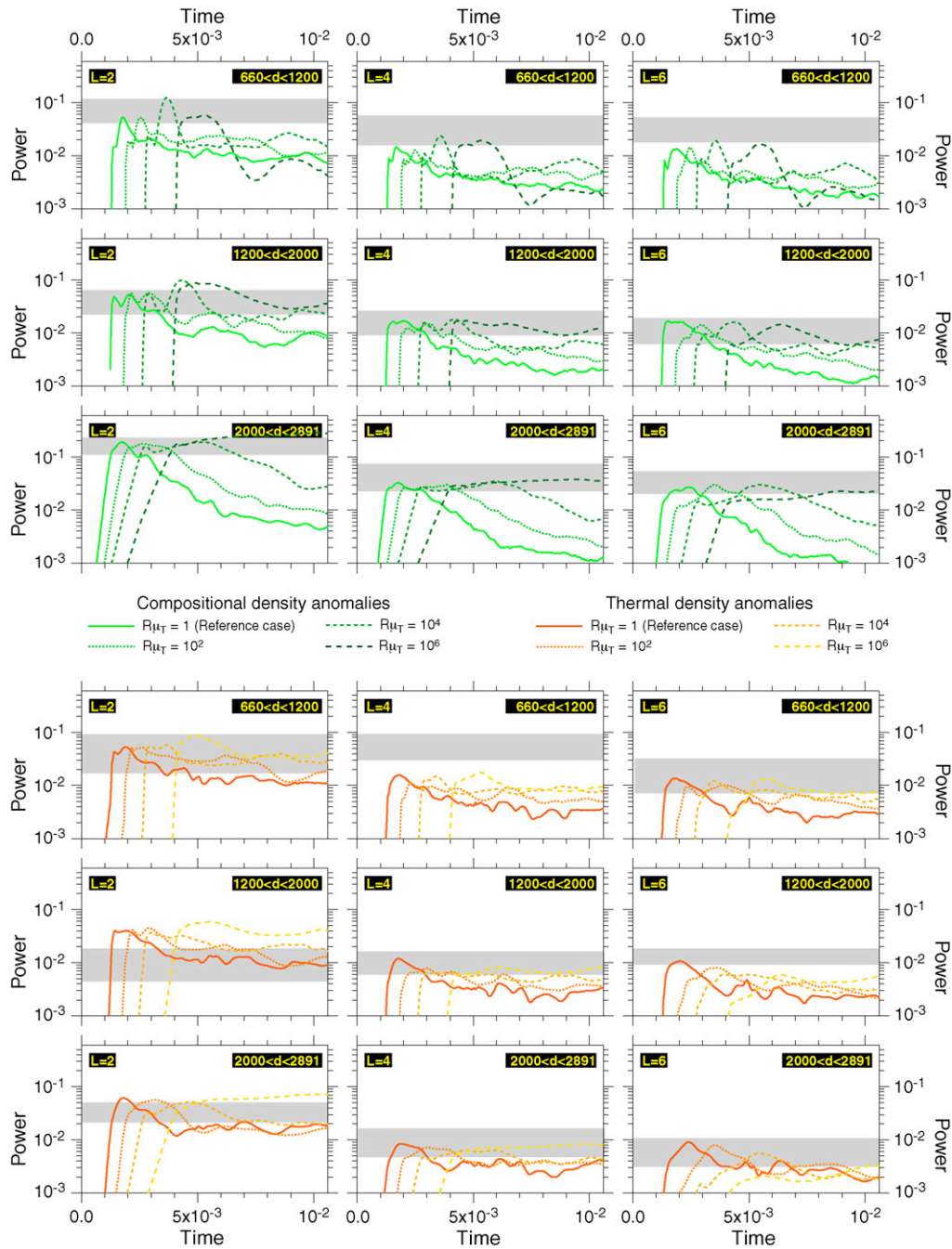
Fig. 11. Same as Fig. 5, but for various values of the thermal viscosity contrast, Rμ_T.

A well-known effect of temperature-dependent viscosity is to weaken the vigor and efficiency of convection, especially when a stagnant lid regime is reached, i.e., for high enough values of Rμ_T (Davaille and Jaupart, 1993; Moresi and Solomatov, 1995; Deschamps and Sotin, 2000). The critical Rayleigh number for the onset of instability increases with Rμ_T, and the heat and flow transfers are less efficient. We observe similar effects in this series of experiments, but because we prescribed a high enough Rayleigh number and included additional complexities that partly balance the thermal viscosity variations, the conditions for a stagnant lid were not reached. The decrease in the vigor and efficiency of convection is however strong enough to maintain pools of dense material at the bottom of the system for periods of time larger than the run duration.

6. Discussion and conclusions

Our goal was to start an extensive exploration of the model space of thermo-chemical convection, and identify models that explain seismic observations well, an important constraint being the presence of large density anomalies in the deep mantle (Ishii and Tromp, 1999; Resovsky and Trampert, 2003; Trampert et al., 2004). For this, we varied the parameters of the viscosity law (other important parameters are explored in a companion paper), and studied their influence on the flow pattern and on the mixing of dense and regular materials. Our approach has however some disadvantages. Linear stability analysis is a powerful tool to analytically describe the results of experiments, but it usually considers two or three parameters at a time. Because we considered too many parameters,

we did not attempt to perform such analysis. For similar reasons, we also did not build any scaling laws.

One may point out that the initial condition that consists in imposing a layer of dense material at the bottom of the system, is somewhat *ad hoc*. Several mechanisms, however, could explain the presence of reservoirs of dense material at the bottom of the mantle, including interactions between the liquid iron of the outer core and the silicates of the lowermost mantle (Knittle and Jeanloz, 1991), and the early differentiation of a magma ocean (Agee and Walker, 1988). Recently, Labrosse et al. (2007) showed that the crystallization of a magma ocean at the base of the mantle (resulting from the sinking of iron-rich droplets) would also result in a reservoir of dense, iron-rich material buried at the bottom of the mantle. Furthermore, this model is consistent with geochemical differences observed between chondrites and mantle rocks (Boyet and Carlson, 2006), and it explains the ultra-low seismic velocities zones (ULVZs) observed locally at the bottom of the mantle (Williams and Garnero, 1996). Another attractive scenario is the recycling of a primitive crust. Recent Sm–Nd data (Caro et al., 2003, 2005) clearly indicate that the oldest crustal rocks observed today were formed from an already depleted mantle, with an age of differentiation around 4.46 Gyr. Further geochemical constraints suggest that the complementary, enriched reservoir crystallized from a magma ocean (Caro et al., 2005) to form an early crust that has then subducted and currently reside in the deep mantle (Boyet and Carlson, 2006). This scenario is supported by recent numerical models of thermo-chemical convection (van Thienen et al., 2004, 2005), which showed that under certain conditions, a primitive crust would delaminate and sink to the bottom of the mantle within about 0.5 Gyr. Earlier models (e.g., Christensen and Hofmann, 1994) also showed that a significant amount of delaminated crust piles up in the deep mantle.

Assuming that a layer of dense material formed early in the Earth's history, a crucial question is to figure out whether this reservoir could survive (at least partially) thermal convection over time intervals comparable to the age of the Earth. Many studies focused on the role of the buoyancy ratio (Davaille, 1999; Tackley, 2002; Samuel and Farnetani, 2003; Zhong and Hager, 2003; van Thienen et al., 2005; Jaupart et al., 2007), which is undoubtedly a major controlling parameter. For values of B larger than a critical value, which varies from one study to another because of differences in the experimental setups and model ingredients, the layer of dense material remains stable over 4.5 Gyr and more. We reach similar conclusions in our companion paper. However, the complete survival a thick ($\delta_{DL} = 0.1D$, and more), stable layer is not desirable, because it does not fit seismic observations (Deschamps et al., 2007; this study). On the contrary, disconnected pools or a layer with strong topography explain seismic tomography better. The 2D-Cartesian model of van Thienen et al. (2005) maintains a layer with strong (up to 10^3 km) topography. 3D-Cartesian models, however, do not predict dense layer with strong topography. For $0.25 \leq B \leq 0.35$ (and $X = 10\%$) the observed patterns are connected ridges of dense material with moderate topography (Tackley, 2002) that does not explain RT246g well (Deschamps et al., 2007), and for $B \geq 0.4$ the layer of dense material fully covers the bottom of the box but has small topography.

As discussed above, it is not unreasonable to impose a basal layer of dense material as initial condition. A more realistic modeling, however, should also include sources and sinks of dense material. This might be achieved by using three types of particles (representing the pyrolitic, MORB, and harzburgitic compositions, respectively) rather than two, and by segregating the material at the top of the system into crustal and residual materials. This more complex modeling may allow part of the dense material entrained upwards to be trapped in the crust, and new MORB material to be recycled in the deep mantle, where it would feed reservoirs of dense material and contribute to their survival.

Cold downwellings are present in our models, but we did not specifically account for the effect of slabs on the stability of the initial layer of dense material and on the distribution of density anomalies. Slab avalanches impacting either a layer or pools of dense material are likely to deflect and destabilize these structures, which may induce strong topography (Kellogg et al., 1999). Furthermore, slabs penetrating in the lower mantle are likely to participate to the density anomalies (thermal and chemical) observed by seismic tomography. For instance, the strong discrepancies that remain between the observed (RT246g) and modeled power spectra of density anomalies in the layer 660–1200 km might be explained by slab stacking below the 660 km discontinuity and down to ~1000 km depth, as observed by regional tomography (Fukao et al., 2001).

Spherical geometry is likely to have a strong effect on the flow pattern. Compared to the 3D-Cartesian case, the stability of the bottom thermal boundary layer is increased, and the ingredients that stabilize the dense layer (large compositional viscosity ratio, large buoyancy ratio) might have more pronounced effects in spherical geometry. Note that the comparison of our 3D-Cartesian models with global seismic tomography models (which are spherically distributed) does not generate additional discrepancies because we converted Fourier spectra into spherical harmonic spectra assuming that the power per surface unit is the same in both expansion (Chevrot et al., 1998).

Due to the simplifications discussed above, the models presented in this study are still far from an accurate description of convection in the real Earth. Our approach, however, allowed identification of possible ingredients for a successful (in the sense that it fits seismic observations well) model of thermo-chemical convection. From this point of view, it is essential for a successful model to maintain pools or layer of dense material with a strong topography in the deep mantle. Too small values of $R\mu_c$ induce fast mixing between dense and regular materials, whereas too large values of $R\mu_c$ induce long-term stability of the dense layer. None of these cases is compatible with seismic observations. A moderate compositional viscosity contrast (typically, between 0.1 and 10) maintain strong density anomalies that fit well RT246g for a long period of time. Possible candidate for the dense material include Fe-rich perovskite and post-perovskite. To date, however, there are no estimates concerning the viscosity of these phases. A large ($\geq 10^2$) viscosity contrast at $d = 660$ km inhibits the mass transfer around this depth, and maintain strong lateral chemical density anomalies over moderate (~1.5 Gyr) time intervals. However, the distributions of these anomalies do not fit RT246g in the long term. The range of value usually assumed for the 660 km viscosity jump (around 10–30) is thus acceptable, provided that other ingredients maintain strong density anomalies in the deep mantle. Large thermal viscosity contrast maintain pools of dense material at the bottom of mantle and significant density anomalies elsewhere in the lower mantle for long periods of time. Again, the distribution of these anomalies fit well those observed by RT246g. It is usually accepted that the mantle viscosity strongly depends on temperature, but this ingredient is sometimes omitted because it induces a stagnant lid at the top of the system. In our case, however, the high Rayleigh number and the additional complexities included in our calculations prevent the development of a stagnant lid at the top of the system.

The main criteria we used to decide the validity of a convection model is its agreement with seismic tomography. It is important to test whether these models also fit other available constraints, in particular the upper mantle geotherm and the surface heat flow (Pollack et al., 1993). Table 2 lists the mean upper mantle potential temperature (T_{UM}) and surface heat flow (Φ_{surf}) averaged over the

Table 2
Predicted upper mantle temperature and surface heat flow for selected cases[a]

Case	T_{UM} (K)[b]	Φ_{surf} (mW/m²)[c]
Reference case	970	77.5
$R\mu_c = 1.0$	920	77.3
$R\mu_c = 10$	820	52.6
$R\mu_c = 10^2$	760	43.4
$R\mu_{660} = 3.0$	1140	100.0
$R\mu_{660} = 3.0 \times 10^2$	840	61.0
$R\mu_T = 10^2$	1140	73.0
$R\mu_T = 10^4$	1280	69.7
$R\mu_T = 10^6$	1280	46.5

[a] Average values over the last Gyr of the run. Possible values for the Earth upper mantle temperature are in the range 1200–1400 K. Surface heat flow strongly varies with location. The compilation of Pollack et al. (1993) proposes a global value around 87 mW/m², with oceanic and continental values around 101 mW/m² and 65 mW/m², respectively.

[b] The upper mantle potential temperature is averaged in the layer $200 \leq d \leq 660$ km $(0.07 \leq z \leq 0.228)$, and scaled with a superadiabatic temperature difference $\Delta T_S = 2500$ K and a surface temperature $T_{surf} = 300$ K. The real temperature can be estimated by assuming that the adiabatic gradient in this layer is 0.4 K/km, i.e., by adding an adiabatic contribution of about 100 K.

[c] Surface heat flow includes a contribution from the adiabatic gradient of temperature. In the reference state we used (Tackley, 1996; Tackley, 1998b), the adiabatic gradient below the surface gradient is about 0.8 K/km. Taking $k_S = 3.0$ W/(m K), the adiabatic contribution to the surface heat flow is thus 2.4 mW/m².

last Gyr of each run for selected cases. The reference case explains well the observed surface heat flow, but has a too low temperature. Both T_{UM} and Φ_{surf} decrease with increasing compositional viscosity contrast, and for $R\mu_c \geq 5$ Φ_{surf} is too low. Increasing the 660 km viscosity contrast has similar effect, but the surface heat flow remains comparable to the observed continental value even for large (3.0×10^2) values of $R\mu_{660}$. With increasing thermal viscosity contrast the upper mantle temperature increases to reasonable values, but in the meantime heat flow decreases and its value for $R\mu_T = 10^6$ is too low. Comparisons with heat flow should however be taken with care because published values (including the compilation by Pollack et al., 1993) are usually not corrected for the crustal heat production, and may thus overestimate the mantle heat flux. In provinces where the crust is thick (e.g., beneath cratons) the crustal contribution to the surface heat flow is likely large, and in some locations the mantle heat flux may not be higher than 15–20 mW/m² (Jaupart and Mareschal, 2007).

We did not run models that simultaneously include high thermal and moderate compositional viscosity contrasts. The combination of these two parameters is likely to induce and maintain strong chemical heterogeneities in the deep mantle. McNamara and Zhong (2004) conducted numerical experiments in spherical geometry with thermal and compositional viscosity contrasts equal to 10^3 and 10^2, respectively, and observed large oscillating plumes of dense material similar to those reported by Davaille (1999). This pattern induces strong topography and might thus explain seismic tomography well.

Finally, more parameters need to be explored. The phase change at $d = 660$ km is endothermic, and for large enough absolute values of its Clapeyron slope, is likely to inhibit the mass transfer, which would help maintaining strong heterogeneities in the lower mantle. Spherical geometry is certainly an important parameter, because it modifies the stability of the hot and cold thermal boundary layers. Finally, the phase transition to post-perovskite, which is not included in the present study, is also likely to influence the flow pattern (Nakagawa and Tackley, 2005), create structures such as double-crossings (Hernlund et al., 2005), and predict specific seismic velocity distributions (Nakagawa and Tackley, 2006). The strong Clapeyron slope of this phase transition implies that cold

material transforms at shallower depths, which might explain the correlation between cold and chemically dense material observed by RT246g (Trampert et al., 2004; Deschamps et al., 2007). In addition, there are indications that the Fe–perovskite transforms to post-perovskite at shallower depths than Mg–perovskite (Ono and Oganov, 2005). Thus, the dense, cold, material observed by RT246g could correspond to pools of Fe-rich post-perovskite resulting, for instance, from the recycling of an early crust.

Acknowledgments

Appendix A. Supplementary data

Supplementary data associated with this article can be found, in the online version, at doi:10.1016/j.pepi.2008.04.016.

References

Agee, C.B., Walker, D., 1988. Mass balance and phase density constraints on early differentiation of chondritic mantle. Earth Planet. Sci. Lett. 90, 144–146.

Boyet, M., Carlson, R.W., 2006. ^{142}Nd evidence for early (>4.53 Ga) global differentiation of the silicate Earth. Science 309, 576–581.

Bunge, H.-P., Richards, M.A., Baumgardner, J.R., 1996. Effects of depth-dependent viscosity on the planform of mantle convection. Nature 379, 436–438.

Caro, G., Bourdon, B., Birck, J.-L., Moorbath, S., 2003. ^{146}Sm–^{142}Nd evidence from Isua metamorphosed sediments for early differentiation of the Earth's mantle. Nature 423, 428–432.

Caro, G., Bourdon, B., Wood, B.J., Corgne, A., 2005. Trace-element fractionation in Hadean mantle generated by melt segregation from a magma ocean. Nature 436, 246–249.

Chevrot, S., Montagner, J.-P., Snieder, R., 1998. The spectrum of tomographic Earth models. Geophys. J. Int. 133, 783–788.

Christensen, U.R., 1984. Heat transport by variable viscosity convection and implications for the Earth's thermal evolution. Phys. Earth Planet. Inter. 35, 264–282.

Christensen, U.R., Hofmann, A., 1994. Segregation of subducted oceanic crust in the convecting mantle. J. Geophys. Res. 99, 19867–19884.

Coltice, N., 2005. The role of convective mixing in degassing the Earth's mantle. Earth Planet. Sci. Lett. 234, 15–25.

Davaille, 1999. Simultaneous generation of hotspots and superswells by convection in a heterogeneous planetary mantle. Nature 402, 756–760.

Davaille, A., Jaupart, C., 1993. Transient high-Rayleigh number thermal convection with large viscosity variations. J. Fluid Mech. 253, 141–166.

Davies, G.F., 2002. Stirring geochemistry in mantle convection models with stiff plates and slabs. Geochem. Cosmochem. Acta 66, 3125–3142.

Deschamps, F., Sotin, C., 2000. Inversion of two-dimensional numerical experiments for a fluid with strongly temperature-dependent viscosity. Geophys. J. Int. 143, 204–218.

Deschamps, F., Sotin, C., 2001. Thermal convection in the outer shell of large icy satellites. J. Geophys. Res. 106, 5107–5121.

Deschamps, F., Trampert, J., 2003. Mantle tomography and its relation to temperature and composition. Phys. Earth Planet. Inter. 140, 277–291.

Deschamps, F., Trampert, J., Tackley, P.J., 2007. Thermo-chemical structure of the lower mantle: seismological evidence and consequences for geodynamics. In: Yuen, D.A., et al. (Eds.), Superplumes: Beyond Plate Tectonics. Springer, pp. 293–320.

Deschamps, F., Tackley, P.J., submitted for publication. Exploring the model space of thermo-chemical convection. II. Physical and compositional parameters. Phys. Earth Planet. Inter.

Ferrachat, S., Ricard, Y., 2001. Mixing properties in the Earth's mantle: effects of the viscosity stratification and oceanic crust segregation. Geochem. Geophys. Geosys. 2, doi:10.1029/2000GC000092.

Forte, A.M., Mitrovica, J.X., 1996. New inferences of mantle viscosity from joint inversion of long-wavelength mantle convection and post-glacial rebound data. Geophys. Res. Lett. 23, 1147–1150.

Forte, A.M., Mitrovica, J.X., 2001. Deep-mantle high-viscosity flow and thermo-chemical structure inferred from seismic and geodynamic data. Nature 410, 1049–1056.

Fukao, Y., Widiyantoro, S., Obayashi, M., 2001. Stagnant slabs in the upper and lower transition regions. Rev. Geophys. 39, 291–323.

Hager, B.H., Richards, M.A., 1989. Long-wavelength variations in Earth's geoid: physical models and dynamical implications. Phil. Trans. Roy. Soc. Lond. A 328, 309–327.

Hernlund, J., Thomas, C., Tackley, P.J., 2005. A doubling of the post-perovskite phase boundary and structure of the Earth's lower mantle. Nature 434, 882–886.

Howard, L.N., 1966. Convection at high Rayleigh number. In: Gortlet, H. (Ed.), Proceedings of the Eleventh International Congress of Applied Mathematics. Springer-Verlag, New York, pp. 1109–1115.

Ishii, M., Tromp, J., 1999. Normal-mode and free-air gravity constraints on lateral variations in velocity and density of Earth's mantle. Science 285, 1231–1236.

Jaupart, C., Mareschal, J.-C., 2007. Heat flow and thermal structure of the lithosphere. In: Schubert, G., et, al. (Eds.), Treatise on Geophysics, vol. 3: Crust and Lithosphere Dynamics. Elsevier, pp. 218–251.

Jaupart, C., Molnar, P., Cottrell, E., 2007. Instability of a chemically dense layer heated from below and overlain by a deep less viscous fluid. J. Fluid Mech. 572, 433–469.

Jellinek, A.M., Manga, M., 2002. The influence of a chemical boundary layer on the fixity, spacing and lifetime of mantle plumes. Nature 418, 760–763.

Karato, S.-I., Wu, P., 1993. The rheology of the upper mantle: a synthesis. Science 260, 771–778.

Karato, S.-I., Karki, B.B., 2001. Origin of lateral variation of seismic wave velocity and density in the deep mantle. J. Geophys. Res. 106, 21771–21783.

Kellogg, L.H., Hager, B.H., van der Hilst, R.D., 1999. Compositional stratification in the deep mantle. Science 283, 1881–1884.

Knittle, E., Jeanloz, R., 1991. Earth's core–mantle boundary: results of experiments at high pressures and temperatures. Science 251, 1438–1443.

Labrosse, S., Hernlund, J.W., Coltice, N., 2007. A crystallizing dense magma ocean at the base of the Earth's mantle. Nature 450, 866–869.

LeBars, M., Davaille, A., 2002. Stability of thermal convection in two superimposed miscible viscous fluids. J. Fluid Mech. 471, 339–363.

McKenzie, D.P., Roberts, J.M., Weiss, N.O., 1974. Convection in the Earth's mantle: towards a numerical simulation. J. Fluid Mech. 62, 465–538.

McNamara, A.K., Zhong, S., 2004. Thermochemical structures within a spherical mantle. J. Geophys. Res. 109, doi:10.1029/2003JB002847.

Moore, D.R., Weiss, N.O., 1973. Two-dimensional Rayleigh–Bénard convection. J. Fluid Mech. 58, 289–312.

Moresi, L.-N., Solomatov, V.S., 1995. Numerical investigation of 2D convection with extremely large viscosity variations. Phys. Fluids 7, 2154–2162.

Nakada, M., Lambeck, K., 1989. Late pleistocene and holocene sea-level change in the Australian region and mantle rheology. Geophys. J. Int. 96, 497–517.

Nakagawa, T., Tackley, P.J., 2005. The interaction between the post-perovskite phase change and a thermo-chemical boundary layer near the core–mantle boundary. Earth Planet. Sci. Lett. 238, 204–216.

Nakagawa, T., Tackley, P.J., 2006. Three-dimensional structures and dynamics in the deep mantle: effects of post-perovskite phase change and deep mantle layering. Geophys. Res. Lett. 33, doi:10.1029/2006GL025719.

Ogawa, M., Schubert, G., Zebib, A., 1991. Numerical simulations of three-dimensional thermal convection in a fluid with strongly temperature-dependent viscosity. J. Fluid Mech. 233, 299–328.

Olson, P., Yuen, D.A., Balsiger, D., 1984. Mixing of passive heterogeneities by mantle convection. J. Geophys. Res. 89, 425–436.

Olson, P., Kincaid, C., 1991. Experiment on the interaction of thermal convection and compositional layering at the base of the mantle. J. Geophys. Res. 96, 4347–4354.

Ono, S., Oganov, A.R., 2005. In situ observations of phase transition between per- ovskite and CaIrO$_3$-type phase in MgSiO$_3$ and pyrolitic mantle composition. Earth Planet. Sci. Lett. 236, 914–932.

Pollack, H.N., Hurter, S.J., Johnson, J.R., 1993. Heat flow from the earth interior: analysis of global data set. Rev. Geophys. 31, 267–280.

Resovsky, J., Trampert, J., 2003. Using probabilistic seismic tomography to test mantle velocity–density relationships. Earth Planet. Sci. Lett. 215, 121–134.

Saltzer, R.L., van der Hilst, R.D., Kárason, H., 2001. Comparing P and S wave hetero- geneity in the mantle. Geophys. Res. Lett. 28, 1335–1338.

Samuel, H., Farnetani, C., 2003. Thermochemical convection and helium concentra- tions in mantle plumes. Earth Planet. Sci. Lett. 207, 39–56.

Smolarkiewicz, P.K., 1984. A fully multidimensional positive definite advection transport algorithm with small implicit diffusion. J. Comput. Phys. 54, 325– 362.

Solomatov, V.S., Moresi, L.-N., 1996. Stagnant lid convection on Venus. J. Geophys. Res. 101, 4737–4753.

Stüben, K., Trottenberg, U., 1982. Multigrids methods: fundamental algorithms, model problem analysis and applications. In: Hackbusch, W., Trottenberg, U. (Eds.), Multigrids Methods. Springer-Verlag, pp. 1–175.

Tackley, P.J., 1996. On the ability of phase transitions and viscosity layering to induce long wavelength heterogeneity in the mantle. J. Geophys. Res. 101, 4737–4753.

Tackley, P.J., 1998a. Self-consistent generation of tectonic plates in three- dimensional mantle convection. Earth Planet. Sci. Lett. 157, 9–22.

Tackley, P.J., 1998b. Three-dimensional simulations of mantle convection with a thermo-chemical CMB boundary layer: D? In: Gurnis, M., et al. (Eds.), The Core–Mantle Boundary Region, Geodynamical Ser. 28. American Geophysical Union, Washington, DC, pp. 231–253.

Tackley, P.J., 2002. Strong heterogeneity caused by deep mantle layering. Geochem. Geophys. Geosys. 3, doi:10.1029/2001GC000167.

Tackley, P.J., King, S.D., 2003. Testing the tracer ratio method for modeling active com- positional fields in mantle convection simulations. Geochem. Geophys. Geosys. 4, doi:10.1029/2001GC000214.

Tackley, P.J., Stevenson, D.J., Glatzmaier, G.A., Schubert, G., 1994. Effects of multiple phase transitions in a three dimensional spherical model of convection in the Earth's mantle. J. Geophys. Res. 99, 15877–15901.

Trampert, J., van der Hilst, R.D., 2005. Towards a quantitative interpretation of global seismic tomography. In: van der Hilst, R.D. (Eds.), Earth's Deep Mantle: Structure, Evolution and Composition, Geophysical Monograph Ser. 160. Amer- ican Geophysical Union, Washington, DC, pp. 47–62.

Trampert, J., Deschamps, F., Resovsky, J.S., Yuen, D.A., 2004. Probabilistic tomography maps significant chemical heterogeneities in the lower mantle. Science 306, 853–856.

van Thienen, P., van den Berg, J.A.P., Vlaar, N.J., 2004. Production and recycling of oceanic crust in the early Earth. Tectonophysics 386, 41–65.

van Thienen, P., van Summeren, J., van der Hilst, R.D., van den Berg, A.P., Vlaar, N.J., 2005. Numerical study of the origin and stability of chemically distinct reser- voirs deep in Earth's mantle. In: van der Hilst, R.D., et al. (Eds.), Earth's Deep Mantle: Structure, Evolution and Composition, Geophysical Monograph Ser. 160. American Geophysical Union, Washington, DC, pp. 117–136.

Weertman, J., 1970. The creep strength of the Earth's mantle. Rev. Geophys. Space Phys. 8, 145–168.

Whitehead, J.A., Luther, D.S., 1975. Dynamics of laboratory diapirs and plume models. J. Geophys. Res. 80, 705–717.

Williams, Q., Garnero, E.J., 1996. Seismic evidence for partial melt at the base of the Earth's mantle. Science 273, 1528–1530.

Zhong, S., Hager, B.H., 2003. Entrainment of a dense layer by thermal plumes. Geo- phys. J. Int. 154, 666–676.